Journal of Power Sources 450 (2020) 227611

Contents lists available at ScienceDirect

Journal of Power Sources

journal homepage: www.elsevier.com/locate/jpowsour

To increase electrochemical performance of electrode material by attaching activated carbon particles on reduced graphene oxide sheets for supercapacitor

Jiaqi Wang [a], Qiang Li [a,*], Cheng Peng [a], Na Shu [b], Liang Niu [a], Yanwu Zhu [b,**]

[a] School of Electronic Science and Applied Physics, Hefei University of Technology, Hefei, Anhui, 230009, China
[b] Hefei National Research Center for Physical Sciences at the Microscale, CAS Key Laboratory of Materials for Energy Conversion & Department of Materials Science and Engineering, University of Science and Technology of China, Hefei, Anhui, 230026, China

HIGHLIGHTS

- RGO-ACP is fabricated by a convenient and scalable method.
- ACP can effectively suppress the aggregation of the rGO sheets.
- RGO-ACP3 increases the specific capacitance of the electrode material by 58.2%.
- RGO-ACP3 delivers high energy density of 11.90 W h kg^{-1} with low cost.

ARTICLE INFO

Keywords:
Reduced graphene oxide
Activated carbon particles
Synergistic effect
Low cost
Supercapacitor

ABSTRACT

A convenient and scalable method is developed to attach the activated carbon particles (ACP) on the surface of reduced graphene oxide (rGO) sheets. The rGO sheets are beneficial for improving the electrochemical performance of the ACP, while ACP can effectively suppress the aggregation of the rGO sheets. Therefore, the symmetric supercapacitor based on this composite (RGO-ACP3) electrode delivers high specific capacitance of 116.88 F g^{-1} at current density of 0.5 A g^{-1} in 1 M H_2SO_4 electrolyte, and has a high capacitance retention of 97.85% after 8000 cycles at 5 A g^{-1}. More importantly, from the perspective of ACP, adding a portion ofrGO to three low-cost ACP can increase the specific capacitance of the electrode material by 58.2%. It also provides high energy density of 11.90 W h kg^{-1} at power density of 469.24 W kg^{-1} in 1 M Na_2SO_4 electrolyte. In addition, the special capacitance contributed byrGO in the RGO-ACP15 reaches up to 541 F g^{-1} at 0.5 A g^{-1} in 1 M H_2SO_4. The results indicate that the synergistic effect betweenrGO sheets and ACP makes RGO-ACP3 a promising low cost electrode material for high performance supercapacitors.

1. Introduction

Supercapacitors are the sustainable electrochemical energy storage system with high power density, short charging time, long cycling lifetime and high safety, which can be applied to pulse electrical equipment, such as uninterruptible power system and auxiliary motive power system. According to the energy storage mechanism, supercapacitors can be divided into three categories: electric double layer capacitors (EDLCs), pseudocapacitors, and hybrid capacitors [1–3]. The energy in the EDLC is stored in an electric double layer formed by physical absorption of electrolyte ions at the electrode/electrolyte interface [4]. While in the pseudocapacitor, a fast Faraday redox reaction occurs at the interface between the electrode and the electrolyte to store energy [5–7]. In hybrid capacitors, both the electric double layer and the Faraday reaction are used to store energy. The power density of EDLC is usually much higher than that of pseudocapacitor and hybrid capacitor, but the energy density of pseudocapacitor and hybrid capacitor is usually higher than that of EDLC. In addition, EDLC has been commercialized, while the other two types are still under development. Carbon materials [3,8] have been widely used in supercapacitors due to their stable physical and chemical properties, large specific surface area (SSA) with hierarchical pores, high electrical conductivity and good

* Corresponding author.
** Corresponding author.
E-mail addresses: qli@hfut.edu.cn (Q. Li), zhuyanwu@ustc.edu.cn (Y. Zhu).

https://doi.org/10.1016/j.jpowsour.2019.227611
Received 4 November 2019; Received in revised form 8 December 2019; Accepted 12 December 2019
Available online 29 January 2020

compatibility with other composite materials [9–12]. Particularly, carbon materials are mainly used for EDLCs, and commonly used to load pseudocapacitor materials, such as nanostructural transition metal oxides, hydroxides and conducting polymers.

rGO has attracted more and more attention in the last decades because of its excellent electronic, thermal, mechanical and optical properties [13]. Due to the special structure of two-dimensional sheets with sp^2-bonded carbon atoms arranged in honeycomb lattice, rGO has outstanding theoretical specific capacitance up to 550 F g^{-1} if its entire theoretical SSA (2630 m^2 g^{-1}) is fully utilized [14]. However, the actual SSA of rGO is usually much lower than its theoretical value, due to the serious aggregation of rGO layers caused by strong π-π interaction between the layers [15], therefore the excellent properties of the individual rGOsheet such as flexibility and high surface area will be lost [16]. One of the effective ways to maintain its high SSA is to attach nanostructural materials on the surface of single rGO sheet before the aggregation of the layers [17–21]. For example, carbon nanoparticles [22,23], metal nanoparticles [24], carbon nanotubes [25], pseudo-capacitive metal oxide nanoparticles [26], conducting polymers [27], etc. have been inserted between the rGO sheets to prevent the aggregation. The synergic effects between rGO sheets and the introduced nanomaterials would also lead to the high electrochemical performance of these composites [8].

Although outstanding electrochemical performances of various relatively new carbon materials including carbon nanotubes, carbon quantum dots, and graphene etc. have been reported, the traditional activated carbon is still a preferred choice for commercial supercapacitors due to its low cost, large SSA and high packing density. Carbon precursors with high carbon content such as fossil fuels [28] and polymers [29] are commonly used to produce activated carbon. In addition, some biomass and industrial wastes that are rich in carbon and easily available can also be used as precursors to fabricate activated carbon, such as human hair [30], bean dregs [31], pistachio shells [32], tobacco rods [33], used methylene blue [34] and printed circuit board [35], etc. The application of these wastes as carbon precursors can reduce the dependence on non-renewable resources, such as fossil fuels, resulting in saving natural resources and environmental protection [36].

In this study, activated carbon particles (ACP) prepared from the waste water purifier was attached on the surface of rGO sheets to prevent the aggregation of the rGO layers, resulting in the improvement of the SSA of the electrode material from 745.06 m^2 g^{-1} (rGO) and 230.86 m^2 g^{-1} (ACP) to 963.69 m^2 g^{-1} (RGO-ACP3, the mass ratio ofrGO:ACP is 1:3). The symmetric supercapacitors based on rGO, ACP and RGO-ACP3 deliver specific capacitance of 107.5, 73.9 and 116.9 F g^{-1} at current density of 0.5 A g^{-1} in 1 M H_2SO_4 electrolyte, respectively. From the perspective of ACP, adding a portion of rGO to three low-cost ACP can increase the specific capacitance of the electrode material by 58.2%. RGO-ACP3 also has high capacitance retention of 97.85% after 8000 cycles at 5 A g^{-1} in 1 M H_2SO_4, and it can provide high energy density of 11.90 W h kg^{-1} at power density of 469.24 W kg^{-1} in 1 M Na_2SO_4 electrolyte. Therefore, the RGO-ACP3 can greatly increase the specific capacitance of activated carbon derived from waste carbon precursor without significantly increasing the material cost, and has potential for practical application. In addition, due to the insertion of ACP between rGO sheets, the special capacitance contributed byrGO in the RGO-ACP15 reaches up to 541 F g^{-1}at 0.5 A g^{-1} in 1 M H_2SO_4.

2. Experimental

2.1. Materials

Graphene oxide (GO) powder was obtained by modified Hummers' method [37]. The carbon filter element (3 M, DWS2500-CN) was purchased from a supermarket in Hefei. Potassium hydroxide (KOH), sulfuric acid (H_2SO_4), sodium sulfate (Na_2SO_4), hydrochloric acid (HCl) and ethanol were analytical pure grade and purchased from Sinopharm Chemical Reagent Co., Ltd. PTFE (10 wt%) was purchased from Sigma-Aldrich. Deionized water was used for all the experiment processes.

2.2. Preparation of rGO sheets attached with ACP (RGO-ACP)

Fig. 1 illustrates the process of preparing RGO-ACP composites. The waste carbon filter element was taken out and dried in an oven at 60 °C for 48 h. The dried filter was cut into small pieces, ground into powder, and then mixed with KOHwithmass ratio of 1:4 (C:KOH) in 40 mL deionized water. The mixture was sonicated for 30 min, and then placed on a rotary evaporator with constant stirring. After the water was evaporated completely, the mixture was placed into a tube furnace, and heated to 900 °C with a rate of 10 °C min^{-1} under nitrogen atmosphere (~100 mL min^{-1}) and kept at 900 °C for 2 h, then cooled naturally to room temperature. The product was washed successively with 5 wt% HCl, ethanol, and deionized water, and then dried at 60 °C overnight. The resulting product was named asACP.The dried filter was also heated directly to 900 °C without KOH activation (named as C900) to check the metal based impurities filtered from city tap water.

0.5 g GO was dispersed and exfoliated homogeneously in 500 mL deionized water through sonication for 2 h to form GO dispersion, and then 2.0 g KOH was added into the dispersion at a mass ratio of GO to KOH of 1:4. The obtained colloidal dispersion was stirring continuously for 1 h to form uniform dispersion, and then moved to a rotary evaporator and stirred at 80 °C overnight till the water was evaporated completely. The obtained paste was dried at 60 °C in the drying oven for 12 h. Then the solid was heated from room temperature to 900 °C with a rate of 10 °C min^{-1} under N_2 flow (~100 mL min^{-1}) and kept at 900 °C for 2 h. After the activation, the product was washed and dried as described above to obtain activated rGO.

In a typical procedure, 0.05 g obtained rGO was uniformly dispersed in 100 mL deionized water through ultrasonication. 0.05 g (0.1, 0.15, 0.25, 0.5, 0.75 and 1 g, respectively) ACP powder was added into the rGO dispersion. The formed homogenous aqueous mixture was stirred under 80 °C vigorously until the water was evaporated. After drying at 60 °C in oven overnight, the as-prepared composites were named as RGO-ACPx (x = 1, 2, 3, 5, 10, 15, and 20, respectively, according to the mass ratio of rGO to ACP).

2.3. Structural characterizations

The morphologies and microstructures of the prepared samples were examined with field emission scanning electron microscope (FESEM, SU8020) and transmission electron microscope (TEM, JEOL-2100), respectively. The structure of the materials was determined by powder X-ray diffraction (XRD, ESCALAB 250xi) with Bragg's angle (2θ) range from 10° to 80°. The surface properties of the samples were analyzed by X-ray photoelectron spectroscopy (XPS, PerkinElmer, ESCALAB 250). Raman spectra (LabRAM HR Evolution) were recorded from 1300 to 2600 cm^{-1}. Pore size characteristics at 77 K of the samples were investigated by a pore size analyzer (Autosorb iQ). The specific surface areas were obtained by Brunauer-Emmett-Teller (BET) method, and the pore size distributions were calculated according to nonlocal density functional theory (NLDFT) model on the basis of slit-like pore geometry.

2.4. Electrochemical measurements

The electrochemical measurements of the samples were carried out with two-electrode symmetrical supercapacitor (as shown in Fig. S1). The electrode contains 80% active material, 15% acetylene black, and 5% polytetrafluoroethylene (PTFE). First, the active material, acetylene black and PTFE were uniformly mixed together in the ethanol solution by a mortar and pestle, and then the mixture was rolled to form a uniform film and punched into disks with diameter of 8 mm. After dried overnight at 110 °C in vacuum, two same disks were assembled into a

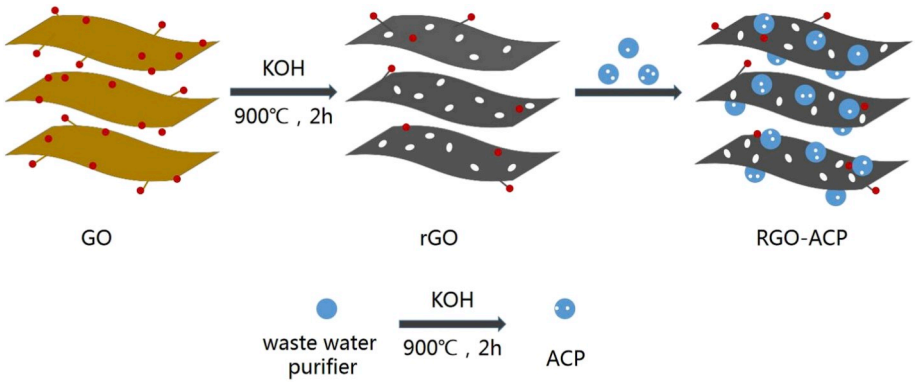

Fig. 1. Schematic of RGO-ACP prepared from waste filter andrGO for supercapacitor.

symmetrical supercapacitor, and the electrolytes used were 1 M H_2SO_4 and 1 M Na_2SO_4, respectively. The mass and size of the electrodes are shown in Table S1.

The cyclic voltammetry (CV), galvanostatic charge-discharge (GCD) and electrochemical impedance spectroscopy (EIS) were measured with electrochemical workstation (CHI660E, Chenhua Instruments, China). In 1 M H_2SO_4 electrolyte, the potential window was controlled within 0–1 V, and CVs were measured under scan rates of 0.5, 0.2, 0.1, 0.05, 0.02 and 0.01 V s^{-1}, GCDs were measured at current densities of 20, 10, 5, 2, 1 and 0.5 A g^{-1}, and the impedances were recorded over 0.01–10^5 Hz with an AC perturbation of 5 mV. The specific capacitance was calculated based on GCD measurements, and the gravimetric capacitance (C_g) and volumetric capacitance (C_v) were calculated by the following equations [38]:

$$C_g = \frac{4I\Delta t}{m\Delta V} \quad (1)$$

$$C_v = \rho C_g \quad (2)$$

$$\rho = \frac{m}{v} \quad (3)$$

$$v = \pi r^2 d \quad (4)$$

where I is the discharge current (A), Δt is the discharge time (s), m is the mass of total active material (g), and ΔV is the operating voltage range (V). ρ (g cm^{-3}), v (cm^3), r (cm) and d (cm) are the density, volume, radius and thickness of the electrode, respectively.

In addition, the special capacitance contributed from just the rGO nanosheets (C_{RGO}) could be calculated by equation (5):

$$\frac{1}{x+1}C_{RGO} + \frac{x}{x+1}C_{ACP} = C_g \quad (5)$$

where x is the different mass ratio of ACP to rGO in the RGO-ACPx composites (x = 1,2,3,5,10,15 and 20, respectively), C_{ACP} is the capacitence of the pure ACP (ACP has low capacitance and good dispersion itself, and ACP is mainly used to disperse rGO. Therefore, we assume that C_{ACP} in the RGO-ACPx composites remains unchanged), C_g is the capacitence of RGO-ACPx composites calculated from equation (1).

The energy densities and power densities were calculated according to the gravimetric capacitance based on the GCD curves by the following equations [38]:

$$E = \frac{C_g \Delta V^2}{8 \times 3.6} \quad (6)$$

$$P = \frac{E \times 3600}{\Delta t} \quad (7)$$

where C_g is the gravimetric capacitance (F g^{-1}), ΔV is the operating voltage range (V), and Δt is the discharge time (s).

3. Results and discussion

3.1. Material characterizations

Fig. 2 shows the images of ACP, rGO, and RGO-ACPx. ACP shows an obvious irregular granular appearance with cluster of particles (Fig. 2a). Both rGO (Fig. 2b) and GO (Fig. S2a) are composed of graphene layers with highly curved or wrinkled surfaces. For RGO-ACP1 (Fig. S2b) and RGO-ACP2 (Fig. S2c), the rGOsheets are re-stacked, because the added ACPis too little to prevent the stacking of sheets. As the proportion of ACP in the composite increases, RGO-ACP3 (Fig. 2c) exhibits a thin sheet-like appearance, and many distinguishable fluffy rGO layers with ACP attached on the surface can be observed. TEM image of RGO-ACP3 (Fig. 2d) shows that ACP attaches uniformly on the surface of therGO sheets. Some rGOsheets in RGO-ACP5 (Fig. 2e) and RGO-ACP10 (Fig. 2f) are almost converted into thick-walled structure with no clearly

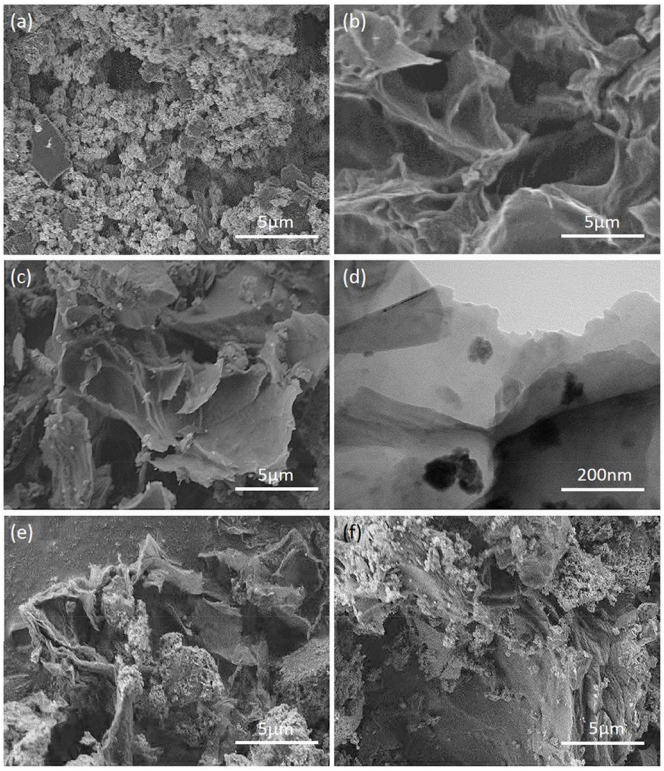

Fig. 2. SEM images of (a)ACP and (b)rGO, (c)SEM and (d)TEM of RGO-ACP3, and SEM of (e)RGO-ACP5 and (f)RGO-ACP10.

distinguishable sheets, due to the high proportion of ACP in these two samples. Therefore, the appropriate ACP content in RGO-ACP3 makes it having unique layered porous microstructure, which is beneficial for thefast transport of electrolyte ions through the electrode.

Fig. 3a shows the XRD patterns of C900, ACP, rGO, and RGO-ACPx. There are some diffraction peaks on the XRD pattern of C900. These peaks are mainly related to the Ti, Ca, Fe metal based compounds (JCPDS: 39–0375, 42–1251, 21–0838)which may be filtered from the city tap water. The rGO has two broad diffraction peaks at about25° and 43.8° which correspond to the (002) diffraction of inorganic carbon and the (100) diffraction of graphitized carbon, respectively. However, the (002)diffraction peak does not appear obviously on the XRD pattern of ACP, indicating the amorphous carbon property of ACP. Due to the adding of ACP into rGO, the (002) diffraction peaks of RGO-ACPx become weaker and shift slightly to the left, which indicates that embedding ACP between rGO sheets reduces the stacking order and density of the rGOlayers [22].

Fig. 3b shows the Raman spectra of ACP, rGO and RGO-ACPx. All Raman spectra show two peaks at about 1350 cm^{-1} and 1590 cm^{-1}, which correspond to the D band and G band of the graphitic carbon, respectively. The D band is attributed to the defect and disordered structure of the sample, while the G band corresponds to the crystalline graphite carbon [39]. The relative intensity ratio (ID/IG) of the D peak to the G peak is usually used to quantify the defects present in the graphite material [40], and the corresponding ID/IG values of samples are showed in Table 1 and Table S2. ACP has a high ID/IG value of 1.04, indicating the large number of defects in ACP due to its amorphous carbon properties. The ID/IG values of RGO-ACPx are all higher than that of rGO (0.89), and as the ACP content increases, the ID/IG value of RGO-ACPx gradually increases from 0.91 (RGO-ACP3) to 1.04 (RGO-ACP10) (Table S2). In addition, the ID/IG value of RGO-ACP10 is

Table 1
Porous property and microstructure of the ACP, rGO and RGO-ACP3 samples.

Materials	S_{BET}[a] (m^2 g^{-1})	S_{micro}[b] (m^2 g^{-1})	$S_{meso/macro}$[c] (m^2 g^{-1})	V_t[d] (cm^3 g^{-1})	V_{micro}[e] (cm^3 g^{-1})	$V_{meso/macro}$[f] (cm^3 g^{-1})	ID/IG
ACP	230.86	110.43	120.43	0.34	0.09	0.26	1.04
rGO	745.06	533.24	211.82	0.63	0.26	0.37	0.89
RGO-ACP3	963.69	835.96	127.73	0.60	0.36	0.24	0.91

[a] Specific surface area.
[b] t-Plot micropore area.
[c] t-Plot external area.
[d] Total pore volume.
[e] t-Plot micropore volume.
[f] t-Plot external volume.

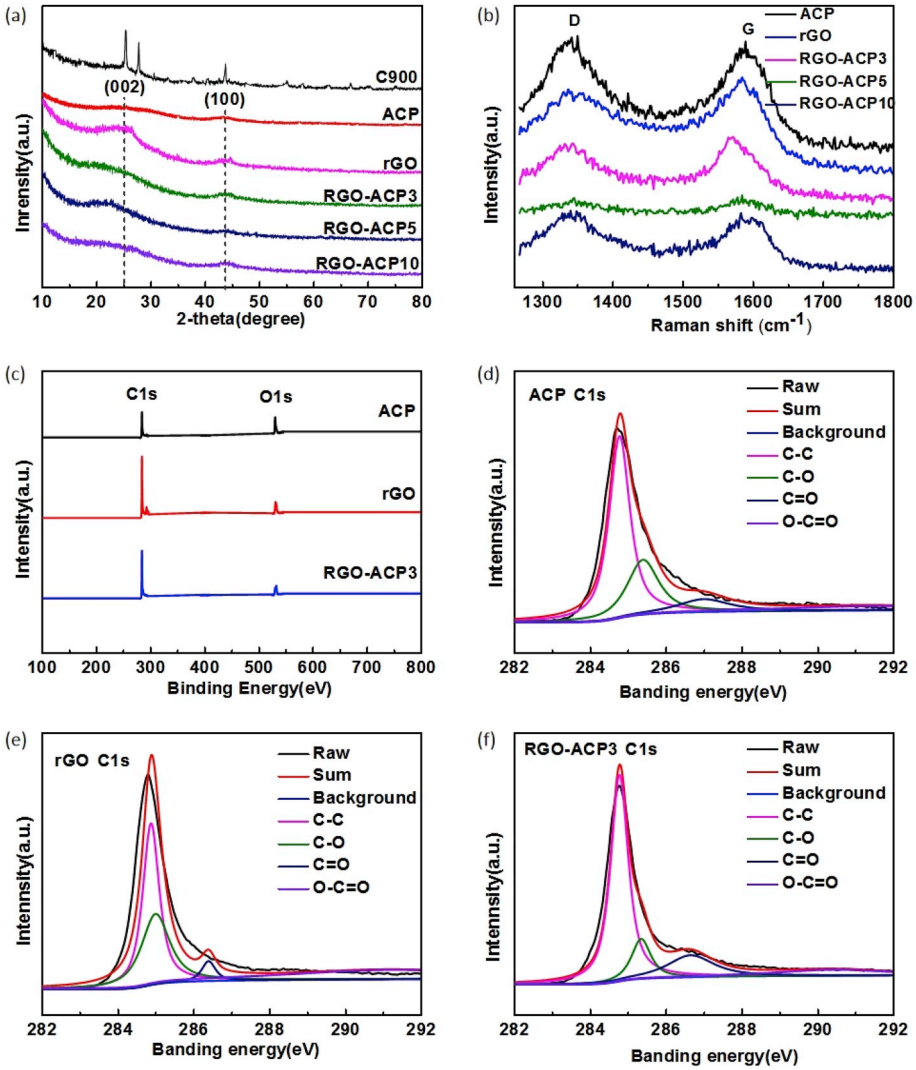

Fig. 3. (a)XRD pattern, (b)Raman spectrum and (c)XPS survey of ACP, rGO and RGO-ACP3. C1 spectra of (d)ACP, (e)rGO, and (f)RGO-ACP3.

relatively close to that of ACP, which may indicate that the rGO sheets in RGO-ACP10 are almost covered by amorphous ACP. Therefore, the RGO-ACP10 mainly reflects the characteristics of amorphous carbon.

The composition and functional groups of ACP, rGO and RGO-ACP3 were examined by XPS. Two peaks were observed on the XPS spectra, and according to the binding energy, they were assigned to C1s and O1s (Fig. 3c). No significant difference in the shape and position of the C1s and O1s peaks of the samples is observed, indicating their similar surface functional groups. In addition, the C1s peaks are broad from 282 to 292 eV, which may be contributed by several carbons in different functional groups (esters, ketones, oximes or carboxyl groups) [41]. The deconvolution results of the C1s peaks of ACP, rGO and RGO-ACP3 are shown in Fig. 3d–f. For RGO-ACP3, the primary peak of C1s appears at 284.7 eV, which is attributed to graphitic carbon. Other smaller peaks were identified as C–O at 285.4 eV, C═O at 286.7 eV, and O–C = O at 290.4 eV [42]. These oxygen-containing functional groups play a significant role in increasing the hydrophilicity of carbon material in aqueous electrolyte, resulting in improving the electrochemical properties [43].

Fig. 4 shows the N_2 adsorption and desorption isotherms and pore size distribution of ACP, rGO and RGO-ACP3. Three samples all have the I/IV type N_2 adsorption-desorption isotherm with hysteresis loops (Fig. 4a), indicating the presence of large number of micropores and mesopores [44,45]. However, their pore size distributions are different (Fig. 4b–d). The micropores of rGO and RGO-ACP3 are obviously higher than that of ACP. Moreover, RGO-ACP3 also has more micropores than rGO. Table 1 shows the pore properties obtained from the N_2 adsorption-desorption isotherm by the BET method. The S_{BET} of ACP, rGO and RGO-ACP3 are 230.86, 745.06, and 963.69 $m^2\ g^{-1}$, respectively. Because of the strong π-π interaction between the rGO layers, the rGO sheets tend to be stacked together, which would make the S_{BET} of rGO much lower than its theoretical value (2630 $m^2\ g^{-1}$). Attaching ACP on the surface of rGO sheets can prevent the aggregation of rGO sheets to some extent, resulting in increasing S_{BET} of rGO. Therefore, the $S_{BET}$of RGO-ACP3is larger than that of rGO. In addition, the increase of S_{BET} from rGO to RGO-ACP3 comes mainly from the increase of S_{micro} (The S_{micro} of rGO and RGO-ACP3 are 533.24 and 835.96 $m^2\ g^{-1}$, respectively, as shown in Table 1). In general, the EDLC of carbon material is mainly determined by micropores which provide active sites to absorb electrolyte ions, while meso/macropores would act as diffusion tunnel for ions transportation in electrode material [46,47]. Therefore, the high S_{BET} with superior pore size distribution of RGO-ACP3 would be beneficial to improve its electrochemical performance.

3.2. Electrochemical characterization

Electrochemical performances of ACP, rGO and RGO-ACPx in 1 M H_2SO_4 are shown in Fig. 5 and Fig. S3. Fig. 5a and Fig. S3a shows the CV curves of ACP, rGO and RGO-ACPx at scan rate of 0.01 V s^{-1}. It is obvious that the CV curves of the samples all exhibit a nearly ideal rectangular shape, indicating that their electrochemical performances are primarily determined by the EDLC [48]. By integrating the area of CV curves, the CV area of RGO-ACP3 is the largest, indicating its highest specific capacitance among the samples. Typical GCD curves of ACP, rGO and RGO-ACPx at current density of 0.5 A g^{-1} are shown in Fig. 5b and Fig. S3b. Symmetric linear charge and discharge curves are observed for the samples, which corresponds to the EDLC charge storage mechanism of carbon materials. Obviously, the capacitive performances of RGO-ACPx are much better than that of ACP (Fig. S3b), and RGO-ACP3 holds the best capacitive performance. Calculated according to the discharge time of GCD curves, the gravimetric (volumetric) capacitance of ACP,rGO, RGO-ACP3 at current density of 0.5 A g^{-1} are 73.9 F g^{-1} (59.1 F cm^{-3}), 107.5 F g^{-1} (96.0 F cm^{-3}), 116.9 F g^{-1} (102.5 F cm^{-3}), respectively. The GCD curve of RGO-ACP3 shows no significant IR drop, while the IR drop is about 0.05 V for rGO (Fig. 5b), which indicates that inserting ACP betweenrGO layers can effectively improve the charge transfer ability of the electrode. Fig. 5c shows the GCD curves of RGO-ACP3 at current densities from 0.5 to 10 A g^{-1}, and they are all triangle shape with no significant IR drop.

The specific capacitances of ACP, rGO and RGO-ACPx in 1 M H_2SO_4 at current densities from 0.5 to 20 A g^{-1} are shown in Fig. 5d and Fig. S3c. Obviously, RGO-ACP3 has the highest specific capacitance among the samples at all current densities. From 0.5 to 20 A g^{-1}, the capacitance retention of ACP, rGO, RGO-ACP3, RGO-ACP5 and RGO-ACP10 are 60.6%, 69.8%, 73.3%, 69.3% and 66.0%, respectively. The

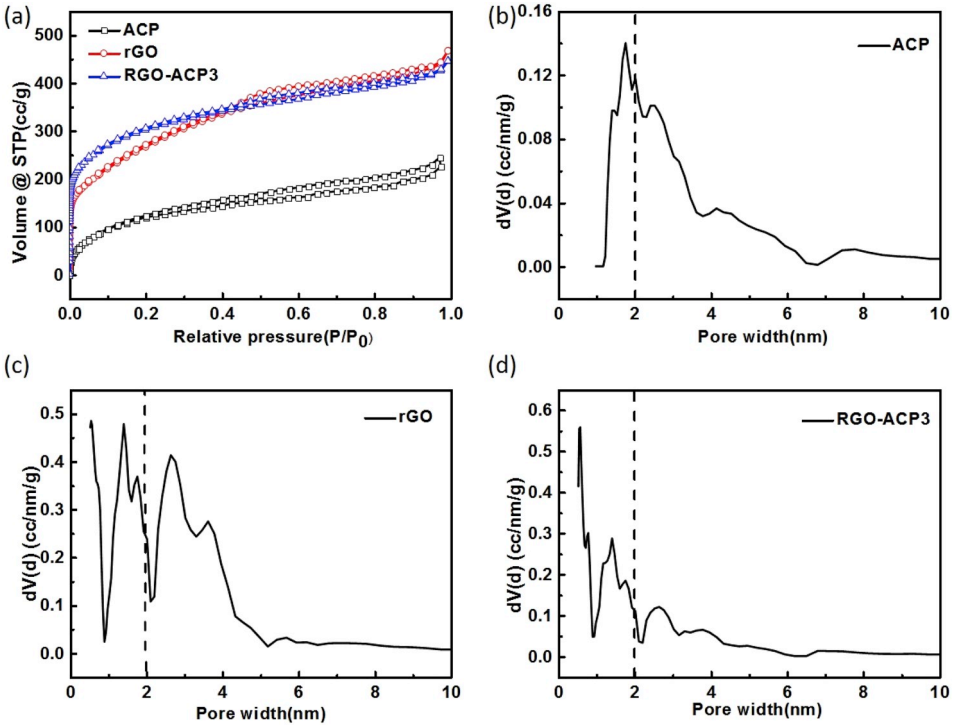

Fig. 4. (a) N_2 adsorption and desorption isotherms of ACP, rGO and RGO-ACP3, and pore size distribution of (b)ACP, (c)rGO and (d)RGO-ACP3.

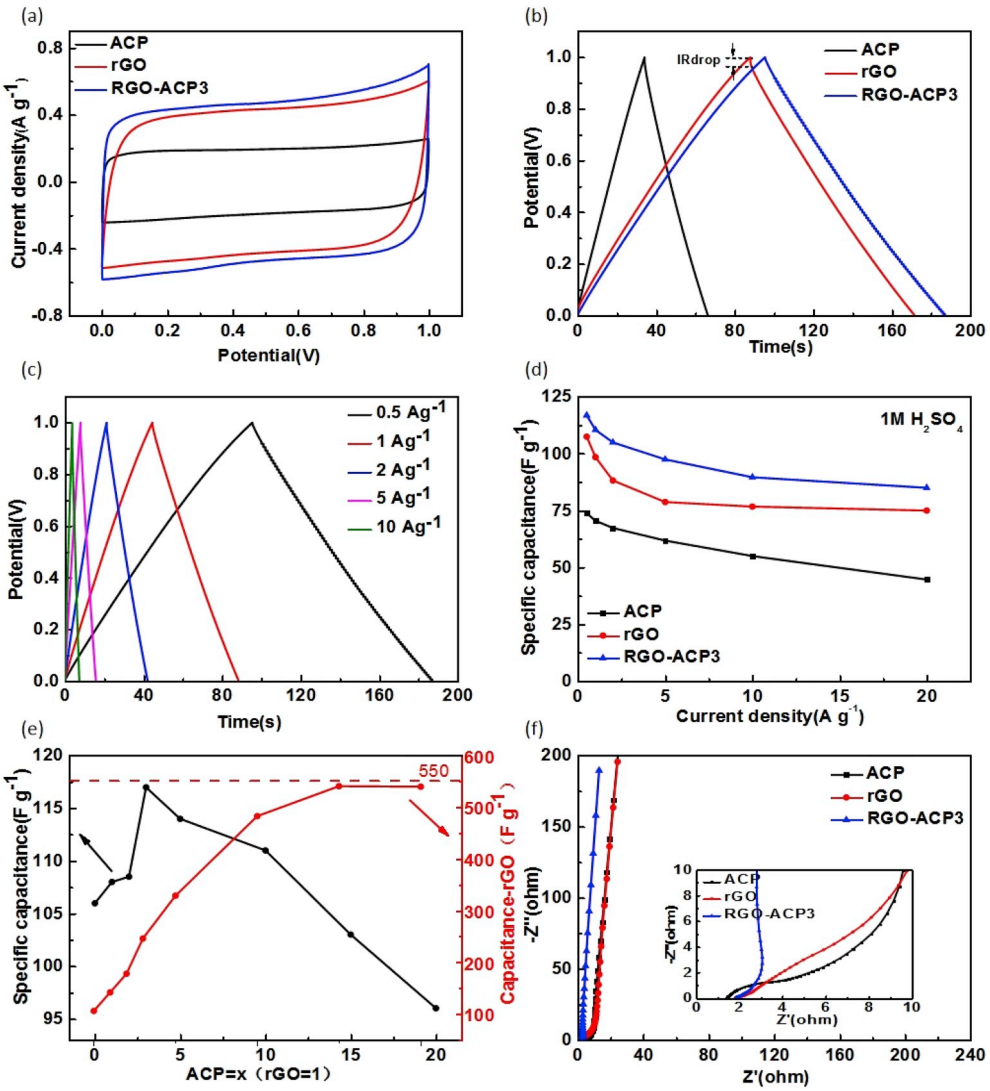

Fig. 5. Electrochemical performance of ACP, rGO and RGO-ACPx measured in 1 M H_2SO_4. (a) CV curves at 0.01 V s^{-1} and (b) Galvanostatic charge-discharge curves at 0.5 A g^{-1} of ACP, rGO and RGO-ACP3. (c) Galvanostatic charge-discharge curves of AGO-ACP3 at different current densities. (d) Gravimetric capacitances calculated from the discharge curves under different current densities of ACP, rGO and RGO-ACP3. (e) Specific capacitance of the RGO-ACPx (x = 0, 1, 2, 3, 5, 10, 15, 20) samples changes with the mass ratio of ACP to rGO at current density of 0.5 A g^{-1}. Black line refers to the specific capacitance calculated from the discharge curves, and red line refers to the capacitance contributed from just rGO. (f) Nyquist plots of ACP, rGO and RGO-ACP3. The inset shows medium-high frequency range. (For interpretation of the references to colour in this figure legend, the reader is referred to the Web version of this article.)

excellent rate capability of RGO-ACP3 (73.3%) is due to its superior layered porous structure. The black line in Fig. 5e (corresponding to the left vertical coordinate) shows the change of specific capacitance (at 0.5 A g^{-1}) with the mass ratio of ACP in the RGO-ACPx. From rGO (107.5 F g^{-1}) to RGO- ACP1 (108 F g^{-1}), RGO-ACP2 (108.5 F g^{-1}) and RGO-ACP3 (116.9 F g^{-1}), the specific capacitance increases sequentially. However, when the mass ratio of ACP is further increased from RGO-ACP3 to RGO-ACP5 (114.6 F g^{-1}), RGO-ACP10 (111.4 F g^{-1}), RGO-ACP15 (103.2 F g^{-1}) and RGO-ACP20 (96 F g^{-1}), the specific capacitance keeps decreasing and approaches that of ACP (73.9 F g^{-1}). The highest specific capacitance of RGO-ACP3 (RGO:ACP = 1:3) among the samples may be due to the following two reasons: (1) Synergetic effect between rGO and ACP. The rGO has high specific surface area with large number of active sites, which is beneficial for improving the electrochemical performance. However, the rGO sheets tend to aggregate because of the strong π-π interaction between them. Attaching ACP on the surface of rGO sheets can effectively prevent the aggregation of the layers, thus maintaining the advantages of the individual rGO sheet. (2) More appropriate mass ratio. For RGO-ACP1 and RGO-ACP2, part of the rGO sheets may be still aggregate together because the amount of ACP is not enough. Therefore, the role of rGO sheets needs to be explored further. However, when the proportion of ACP is too high (RGO-ACP5, RGO-ACP10, RGO-ACP15, RGO-ACP20), the low capacitance of ACP would lower the capacitance of the entire electrode material, even if the rGO sheets were fully used to store electrolyte ions. The attaching of appropriate mass of ACP tightly and uniformly on therGO sheets makes RGO-ACP3 having unique layered porous microstructure, which is beneficial for thefast transport of electrolyte ions through the electrode material.

In addition, assuming that the specific capacitance of ACP in the RGO-ACPx keeps constant, the specific capacitance (C_{RGO}) contributed from just therGO sheets can be calculated by equation (5), as shown in the red line in Fig. 5e (corresponding to the right vertical coordinate). It is shown that the specific capacitance contributed byrGOsheets increases with the increase of ACP ratio in RGO-ACPx, and it reaches a maximum value of 541 F g^{-1} in RGO-ACP15 (the theoretical specific capacitance ofrGO is 550 F g^{-1}). Although the above assumption ignores the possible change of the specific capacitance contributed by ACP in RGO-ACPx, the result still indicates that there are less and less rGO sheets stacking together as the ACP ratio increasing, resulting in the utilization of the excellent properties of more individual rGO sheets such as high specific surface area and large numbers of active sites.

To further understand the electrochemical performance of the samples, EIS measurements were performed on the samples (The Nyquist plots in Fig. 5f and Fig. S2d.). In the low frequency region, the almost vertical lines indicate an ideal capacitive behavior of the samples. The inset in Fig. 5f shows the medium-high frequency region of nyquist plots of ACP, rGO and RGO-ACP3. The equivalent serial resistances (ESR, the intercept of Nyquist plot with real axis) of this three samples are all very

low (about 2 Ω), indicating their excellent charge transfer capability [49,50]. However, RGO-ACP3 has a much shorter length of 45° sloped line (warburg impedance) than those of ACP and rGO, which indicates that the electrode of RGO-ACP3 has the most excellent electrolyte ions diffusion capability in 1 M H_2SO_4 electrolyte among the samples [51]. The lowest warburg impedance of RGO-ACP3 among the samples is mainly due to its layered porous microstructure with appropriate ACP ratio which facilitates the diffusion of electrolyte ions in the electrode.

According to equation (6), a wide operating voltage will increase the energy density of the supercapacitor. Therefore, the RGO-ACP3 based symmetrical supercapacitor was tested with 1 M Na_2SO_4 as electrolyte to increase the operating voltage [52]. The inset of Fig. 6a shows the CV curves of RGO-ACP3 at different voltage windows from 1.2 to 1.8 V at 0.01 V s^{-1}. Until to 1.6 V, the CV curves can keep rectangular shape, indicating that this supercapacitor can be operated stably from 0 to 1.6 V in 1 M Na_2SO_4. The operating voltage reaching 1.6 V in neutral electrolyte is attributed to the higher over-potential for di-hydrogen evolution than in acidic or basic electrolyte [53]. The CV curves from 0 to 1.6 V at different scan rates all keep rectangular shape (Fig. 6a). The GCD curves from 0 to 1.6 V at different current densities all keep symmetrical triangle (Fig. 6b). Both CV curves and GCD curves indicate the typical EDLC behavior of RGO-ACP3. The GCD curve at 0.5 A g^{-1} shows IR drop of about 0.04 V, indicating the increase of charge transfer resistance in 1 M Na_2SO_4compared to 1 M H_2SO_4. Fig. 6c shows the specific capacitances of RGO-ACP3 at different current densities. The capacitance drops from 95.2 F g^{-1} at 0.5 A g^{-1} to 66.4 F g^{-1} at 20 A g^{-1} with a capacitance retention of 69.72%, indicating an excellent rate capability of RGO-ACP3 in 1 M Na_2SO_4. Fig. 6d shows that RGO-ACP3 also has good capacitive behavior and low ESR in 1 M Na_2SO_4. However, the 45° sloped line (warburg impedance) in 1 M Na_2SO_4 (inset of Fig. 6d) is obviously longer than that in 1 M H_2SO_4 (inset of Fig. 5f), indicating the larger ions diffusion resistance of electrode material in 1 M Na_2SO_4 than that in 1 M H_2SO_4.

Fig. 7a shows the Ragone plot of RGO-ACP3 in 1 M H_2SO_4 and 1 M Na_2SO_4 electrolyte, respectively. In 1 M H_2SO_4, RGO-ACP3 has an energy density of 8.12 W h kg^{-1} at power density of 312.5 W kg^{-1}. Due to the wider operating voltage window (1.6 V) in 1 M Na_2SO_4 electrolyte, the energy density increases to 11.9 W h kg^{-1} at power density of 469.24 W kg^{-1}. As the power density increases to larger than 3000 W kg^{-1}, the energy density in 1 M Na_2SO_4 decreases faster than that in 1 M H_2SO_4, due to the higher ions diffusion resistance of Na^+ in the RGO-ACP3 electrode. After8000charge-discharge cycles at 5 A g^{-1} in 1 M H_2SO_4,RGO-ACP3 maintained a high capacitance retention of 97.85% (Fig. 7b). There was no significant distortion in the shape of the GCD curves during the cycling (inset of Fig. 7b), indicating its excellent electrochemical stability. Therefore, the stable layered porous microstructure of RGO-ACP3 during cycling process with high energy density makes it a potential candidate for practical application.

4. Conclusions

In summary, RGO-ACP composites were successfully prepared by attaching the ACP on the surface of rGO sheets. The symmetric supercapacitor based on RGO-ACP3 has a gravimetric capacitance of 116.88 F g^{-1} and a volumetric capacitance of 102.53 F cm^{-3} at current density of 0.5 A g^{-1} and high capacitance retention of 97.85% after 8000 cycles at 5 A g^{-1} in 1 M H_2SO_4 electrolyte. This supercapacitor also provides a high energy density of 11.9 W h kg^{-1} at power density of 469.24 W kg^{-1} in 1 M Na_2SO_4. More importantly, from the perspective of ACP, adding a portion of rGO to three low-cost ACP can increase the specific capacitance of the electrode material by 58.2%.The excellent electrochemical performance RGO-ACP3 is due to the synergic effect between ACP and rGO.Therefore, this research provides a convenient and scalable method for not only increasing the electrochemical performance of waste materials derived activated carbon but also preventing the aggregation of rGO sheets when used for practical application. In addition, the specific

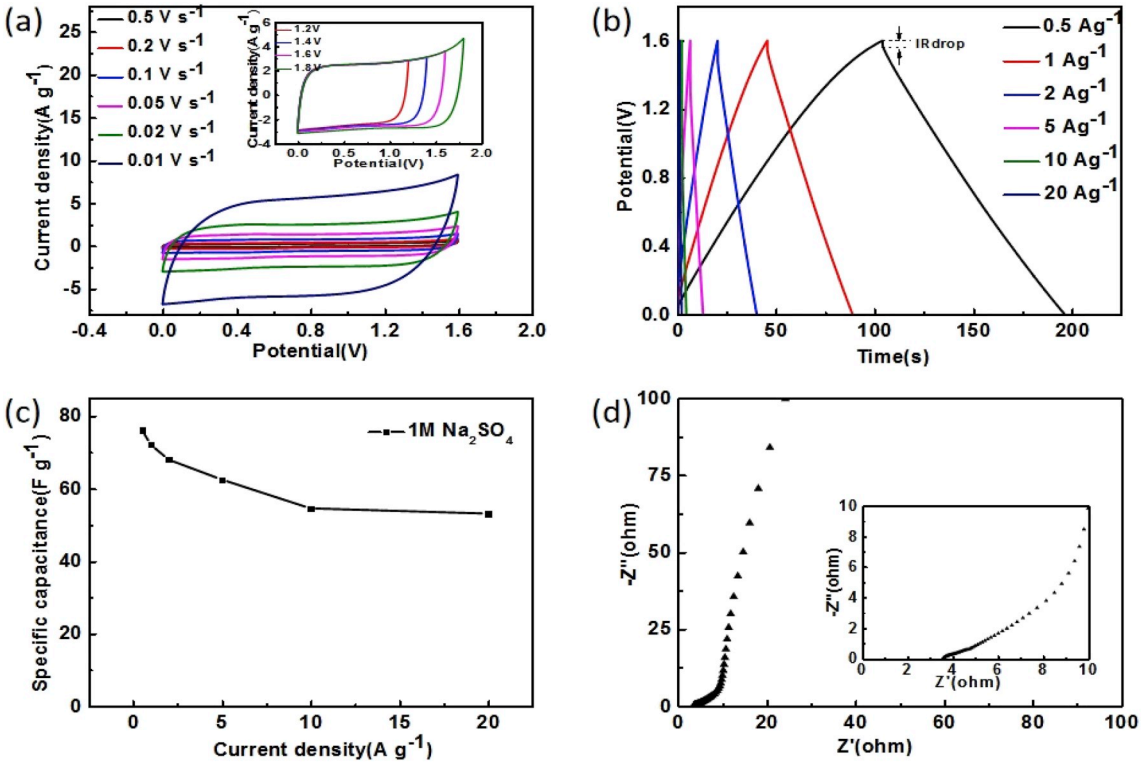

Fig. 6. Electrochemical performance of RGO-ACP3 measured in 1 M Na_2SO_4. (a)CV curves of RGO-ACP3 at different scan rates from 0 to 1.6 V. The inset shows CV curves of RGO-ACP3 at different voltage window at 0.01 V s^{-1}. (b)Galvanostatic charge-discharge curves of RGO-ACP3 at different current densities. (c)Gravimetric capacitances of RGO-ACP3 calculated from the discharge curves under different current densities. (d)Nyquist plots of RGO-ACP3. The inset shows high frequency range.

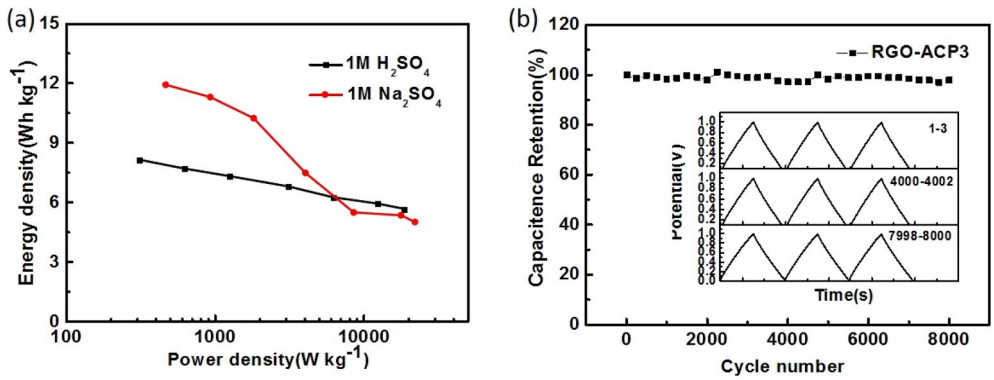

Fig. 7. (a)Ragone plots of RGO-ACP3 in 1 M H_2SO_4 and 1 M Na_2SO_4, respectively. (b)Cycling stability of RGO-ACP3 in 1 M H_2SO_4 for 8000 cycles at 5 A g^{-1}. The inset shows the detailed GCD curves of the start, middle and last three cycles.

capacitance contributed byrGO in the RGO-ACP15 reaches up to 541 F g^{-1} at 0.5 A g^{-1} in 1 M H_2SO_4.

Declaration of competing interest

The authors declare that they have no known competing financial interests or personal relationships that could have appeared to influence the work reported in this paper.

Acknowledgements

This work was funded by the Natural Science Foundation of China (51772282, 51322204) and Specialized Research Fund for the Doctoral Program of Higher Education of China (No. 20120111120009).

Appendix A. Supplementary data

Supplementary data to this article can be found online at https://doi.org/10.1016/j.jpowsour.2019.227611.

References

[1] W. Qian, J. Yan, Z. Fan, Carbon materials for high volumetric performance supercapacitors: design, progress, challenges and opportunities, Energy Environ. Sci. 9 (2016) 729–762.
[2] L. Wang, Y.Z. Han, X. Feng, J.W. Zhou, P.F. Qi, B. Wang, Metal-organic frameworks for energy storage: batteries and supercapacitors, Coordin. Chen. Rev. 307 (2016) 361–381.
[3] C.L. Long, D.P. Qi, T. Wei, J. Yan, L.L. Jiang, Z.J. Fan, Nitrogen-doped carbon networks for high energy density supercapacitors derived from polyaniline coated bacterial cellulose, Adv. Funct. Mater. 24 (2014) 3953–3961.
[4] R. Kötz, M. Carlen, Principles and applications of electrochemical capacitors, Electrochim. Acta 45 (2000) 2483–2498.
[5] H.Y. Ma, D.B. Kong, Y. Xu, X.Y. Xie, Y. Tao, Z.C. Xiao, W. Lv, H.D. Jang, J. X. Huang, Q.H. Yang, Disassembly-reassembly approach to RuO_2/graphene composites for ultrahigh volumetric capacitance supercapacitor, Small 13 (2017) 1701026.
[6] N. Choudhary, C. Li, J. Moore, N. Nagaiah, L. Zhai, Y. Jung, J. Thomas, Asymmetric supercapacitor electrodes and devices, Adv. Mater. 29 (2017) 1605336.
[7] M. Yu, Z.L. Wang, Y. Han, Y.X. Tong, X.H. Lu, S.H. Yang, Recent progress in the development of anodes for asymmetric supercapacitors, J. Mater. Chen. A 4 (2016) 4634–4658.
[8] K.L. Sun, S.S. Yu, Z.L. Hu, Z.H. Li, G.T. Lei, Q.Z. Xiao, Y.H. Ding, Oxygen-containing hierarchically porous carbon materials derived from wild jujube pit for high-performance supercapacitor, Electrochim. Acta 231 (2017) 417–428.
[9] M.J. Zhi, C.C. Xiang, J.T. Li, M. Li, N.Q. Wu, Nanostructured carbon-metal oxide composite electrodes for supercapacitors: a review, Nanoscale 5 (2013) 72–88.
[10] Y. Liu, Y.L. Ying, Y.Y. Mao, L. Gu, Y.W. Wang, X.S. Peng, CuO nanosheets/rGO hybrid lamellar films with enhanced capacitance, Nanoscale 5 (2013) 9134–9140.
[11] Y. Liu, W. Wang, Y.L. Ying, Y.W. Wang, X.S. Peng, Binder-free layered Ti_3C_2/CNTs nanocomposite anodes with enhanced capacity and long-cycle life for lithium-ion batteries, Dalton Trans. 44 (2015) 7123–7126.
[12] Y. Liu, X.Y. Cai, B.F. Luo, M. Yan, J.H. Jiang, W.D. Shi, MnO_2 decorated on carbon sphere intercalated graphene film for high-performance supercapacitor electrodes, Carbon 107 (2016) 426–432.
[13] H. Su, H.T. Zhang, F.Y. Liu, F.J. Chun, B.B. Zhang, X. Chu, H.C. Huang, W.L. Deng, B.N. Gu, H.P. Zhang, X.T. Zheng, M.H. Zhu, W.Q. Yang, High power supercapacitors based on hierarchically porous sheet-like nanocarbons with ionic liquid electrolytes, Chen. Eng. J. 322 (2017) 73–81.
[14] H.X. Chang, H.K. Wu, Graphene-based nanocomposites: preparation, functionalization, and energy and environmental applications, Energ. Environ. Sci. 6 (2013) 3483–3507.
[15] M.D. Stoller, S.J. Park, Y.W. Zhu, J. An, R.S. Ruoff, Graphene-based ultracapacitors, Nano Lett. 8 (2008) 3498–3502.
[16] W.J. Ma, S.H. Chen, S.Y. Yang, W.P. Chen, Y.H. Cheng, Y.W. Guo, S.J. Peng, S. Ramakrishna, M. Zhu, Hierarchical MnO_2 nanowire/graphene hybrid fibers with excellent electrochemical performance for flexible solid-state supercapacitors, J. Power Sources 306 (2016) 481–488.
[17] J.Y. Luo, H.D. Jang, J.X. Huang, Effect of sheet morphology on the scalability of graphene-based ultracapacitors, ACS Nano 7 (2013) 1464–1471.
[18] M.X. Wang, Q. Liu, H.F. Sun, E.A. Stach, H.Y. Zhang, L. Stanciu, J. Xie, Preparation of high-surface-area carbon nanoparticle/graphene composites, Carbon 50 (2012) 3845–3853.
[19] J. Yan, T. Wei, B. Shao, F.Q. Ma, Z.J. Fan, M.L. Zhang, C. Zheng, Y.C. Shang, W. Z. Qian, F. Wei, Electrochemical properties of graphene nanosheet/carbon black composites as electrodes for supercapacitors, Carbon 48 (2010) 1731–1737.
[20] Q. Cheng, J. Tang, J. Ma, H. Zhang, N. Shinya, L.C. Qin, Graphene and carbon nanotube composite electrodes for supercapacitors with ultra-high energy density, Phys. Chem. Chem. Phys. 13 (2011) 17615–17624.
[21] Y. Wang, Y.P. Wu, Y. Huang, F. Zhang, X. Yang, Y.F. Ma, Y.S. Chen, Preventing graphene sheets from restacking for high-capacitance performance, J. Phys. Chem. C 115 (2011) 23192–23197.
[22] D.Q. Liu, Z. Jia, D.L. Wang, Preparation of hierarchically porous carbon nanosheet composites with graphene conductive scaffolds for supercapacitors: an electrostatic-assistant fabrication strategy, Carbon 100 (2016) 664–677.
[23] C. Zheng, X.F. Zhou, H.L. Cao, G.H. Wang, Z.P. Liu, Synthesis of porous graphene/activated carbon composite with high packing density and large specific surface area for supercapacitor electrode material, J. Power Sources 258 (2014) 290–296.
[24] Y.C. Si, E.T. Samulski, Exfoliated graphene separated by platinum nanoparticles, Chem. Mater. 20 (2008) 6792–6797.
[25] Z.D. Huang, B. Zhang, S.W. Oh, Q.B. Zheng, X.Y. Lin, N. Yousefi, J.K. Kim, Self-assembled reduced graphene oxide/carbon nanotube thin films as electrodes for supercapacitors, J. Mater. Chem. 22 (2012) 3591–3599.
[26] H.J. Choi, S.M. Jung, J.M. Seo, D.W. Chang, L.M. Dai, J.B. Baek, Graphene for energy conversion and storage in fuel cells and supercapacitors, Nano Energy 1 (2012) 534–551.
[27] N.A. Kumar, H.J. Choi, Y.R. Shin, D.W. Chang, L.M. Dai, J.B. Baek, Polyaniline-grafted reduced graphene oxide for efficient electrochemical supercapacitors, ACS Nano 6 (2012) 1715–1723.
[28] M.X. Guo, J.X. Guo, D.Z. Jia, H.Y. Zhao, Z.P. Sun, X.L. Song, Y.H. Li, Coal derived porous carbon fibers with tunable internal channels for flexible electrodes and organic matter absorption, J. Mater. Chem. 3 (2015) 21178–21184.
[29] K.H.S. Lessa, Y. Zhang, G. Zhang, F. Xiao, S. Wang, Conductive porous sponge-like ionic liquid-graphene assembly decorated with nanosized polyaniline as active electrode material for supercapacitor, J. Power Sources 302 (2016) 92–97.
[30] W.J. Qian, F.X. Sun, Y.H. Xu, L.H. Qiu, C.H. Liu, S.D. Wang, F. Yan, Human hair-derived carbon flakes for electrochemical supercapacitors, Energy Environ. Sci. 7 (2014) 379–386.
[31] Y. Teng, E.H. Liu, R. Ding, K. Liu, R.H. Liu, L. Wang, Z. Yang, H.X. Jiang, Bean dregs-based activated carbon/copper ion supercapacitors, Electrochim. Acta 194 (2016) 394–404.
[32] J.D. Xu, Q.M. Gao, Y.L. Zhang, Y.L. Tan, W.Q. Tian, L.H. Zhu, L. Jiang, Preparing two-dimensional microporous carbon from Pistachio nutshell with high areal capacitance as supercapacitor materials, Sci. Rer-uk. 4 (2014) 5545.
[33] P. Kleszyk, P. Ratajczak, P. Skowron, J. Jagiello, Q. Abbas, E. Frackowiak, F. Béguin, Carbons with narrow pore size distribution prepared by simultaneous carbonization and self-activation of tobacco stems and their application to supercapacitors, Carbon 81 (2015) 148–157.

[34] J. Yin, Y.Q. Zhu, X. Yue, L. Wang, H. Zhu, C.Y. Wang, From environmental pollutant to activated carbons for high-performance supercapacitors, Electrochim. Acta 201 (2016) 96–105.
[35] R.R. Rajagopal, L.S. Aravinda, R. Rajarao, B.R. Bhat, V. Sahajwalla, Activated carbon derived from non-metallic printed circuit board waste for supercapacitor application, Electrochim. Acta 211 (2016) 488–498.
[36] G.J. Li, Q. Li, J.L. Ye, G.S. Fu, J.J. Han, Y.W. Zhu, Activated carbon from the waste water purifier for supercapacitor application, J. Solid State Electrochem. 21 (2017) 3169–3177.
[37] W.S. Hummers, R.E. Offeman, Preparation of graphitic oxide, J. Am. Chem. Soc. 80 (1958), 1339-1339.
[38] C. Xu, B. Xu, Y. Gu, Z. Xiong, J. Sun, X.S. Zhao, Graphene-based electrodes for electrochemical energy storage, Energy Environ. Sci. 6 (2013) 1388–1414.
[39] C.C. Su, C.J. Pei, B.X. Wu, J.F. Qian, Y.W. Tan, Highly doped carbon nanobelts with ultrahigh nitrogen content as high-performance supercapacitor materials, Small 13 (2017) 1700834.
[40] A.C. Ferrari, J. Robertson, Interpretation of Raman spectra of disordered and amorphous carbon, Phys. Rev. B 61 (2000) 14095.
[41] Y.W. Zhu, S. Murali, W.W. Cai, X.S. Li, J.W. Suk, J.R. Potts, R.S. Ruoff, Graphene and graphene oxide: synthesis, properties, and applications, Adv. Mater. 22 (2010) 3906–3924.
[42] W.H. Lee, J.Y. Kima, Y.K. Koa, P.J. Reucrofta, J.W. Zondlob, Surface analysis of carbon black waste materials from tire residues, Appl. Surf. Sci. 141 (1999) 107–113.
[43] W.H. Lee, P.J. Reucroft, Vapor adsorption on coal and wood-based chemically activated carbons: (I) surface oxidation states and adsorption of H_2O, Carbon 37 (1999) 7–14.
[44] C.T. Hsieh, H. Teng, Influence of oxygen treatment on electric double-layer capacitance of activated carbon fabrics, Carbon 40 (2002) 667–674.
[45] K.S.W. Sing, Reporting physisorption data for gas/solid systems with special reference to the determination of surface area and porosity (Recommendations 1984), Pure Appl. Chem. 57 (1985) 603–619.
[46] L. Sun, C.G. Tian, M.T. Li, X.Y. Meng, L. Wang, R.H. Wang, J. Yin, H.G. Fu, From coconut shell to porous graphene-like nanosheets for high-power supercapacitors, J. Mater. Chem. 1 (2013) 6462–6470.
[47] Y.C. Liu, B.B. Huang, X.X. Lin, Z.L. Xie, Biomass-derived hierarchical porous carbons: boosting the energy density of supercapacitors via an ionothermal approach, J. Mater. Chem. 5 (2017) 13009–13018.
[48] O. Barbieri, M. Hahn, A. Herzog, R. Kötz, Capacitance limits of high surface area activated carbons for double layer capacitors, Carbon 43 (2005) 1303–1310.
[49] B.Q. Qian, G. Wang, Z. Ling, Q. Dong, T.T. Wu, X. Zhang, J.S. Qiu, Sulfonated graphene as cation-selective coating: a new strategy for high-performance membrane capacitive deionization, Adv. Mater. Interfaces 2 (2015) 1500372.
[50] Q. Cheng, J. Tang, J. Ma, H. Zhang, N. Shinya, L.C. Qin, Graphene and nanostructured MnO_2 composite electrodes for supercapacitors, Carbon 49 (2011) 2917–2925.
[51] X.X. Sun, P. Cheng, H.J. Wang, H. Xu, L.Q. Dang, Z.H. Liu, Z.B. Lei, Activation of graphene aerogel with phosphoric acid for enhanced electrocapacitive performance, Carbon 92 (2015) 1–10.
[52] A.Izadi Najafabadi, S. Yasuda, K. Kobashi, T. Yamada, D.N. Futaba, H. Hatori, M. Yumura, S. Iijima, K. Hata, Extracting the full potential of single-walled carbon nanotubes as durable supercapacitor electrodes operable at 4 V with high power and energy density, Adv. Mater. 22 (2010) E235–E241.
[53] L. Demarconnay, E. Raymundo-Piñero, F. Beguin, A symmetric carbon/carbon supercapacitor operating at 1.6 V by using a neutral aqueous solution, Electrochem. Commun. 12 (2010) 1275–1278.